

### HIV-2 Immature Particle Morphology Provides Insights into Gag Lattice Stability and Virus Maturation

Nathaniel Talledge <sup>1,2,3†</sup>, Huixin Yang <sup>1,4†</sup>, Ke Shi <sup>1,5†</sup>, Raffaele Coray <sup>6</sup>, Guichuan Yu <sup>7,8</sup>, William G. Arndt <sup>1,9</sup>, Shuyu Meng <sup>1,10</sup>, Gloria C. Baxter <sup>1,3,11</sup>, Luiza M. Mendonça <sup>1,2,5,9</sup>, Daniel Castaño-Díez <sup>12</sup>, Hideki Aihara <sup>1,5,9</sup>, Louis M. Mansky <sup>1,2,3,4,9,10\*</sup> and Wei Zhang <sup>1,2,3,8\*</sup>

- 1 Institute for Molecular Virology, University of Minnesota Twin Cities, Minneapolis, MN 55455, USA
- 2 Department of Diagnostic and Biological Sciences, School of Dentistry, University of Minnesota Twin Cities, Minneapolis, MN 55455. USA
- 3 Masonic Cancer Center, University of Minnesota Twin Cities, Minneapolis, MN 55455, USA
- 4 Comparative Molecular Biosciences Graduate Program, University of Minnesota Twin Cities, St. Paul, MN 55108, USA
- 5 Department of Biochemistry, Molecular Biology and Biophysics, University of Minnesota Twin Cities, Minneapolis, MN 55455, USA
- 6 BioEM Lab, Biozentrum, University of Basel Basel, Switzerland
- 7 Minnesota Supercomputing Institute, Office of the Vice President for Research, University of Minnesota Twin Cities, Minneapolis, MN 55455. USA
- 8 Characterization Facility, College of Sciences and Engineering, University of Minnesota Twin Cities, Minneapolis, MN 55455, USA
- 9 Biochemistry, Molecular Biology and Biophysics Graduate Program, University of Minnesota Twin Cities, Minneapolis, MN 55455. USA
- 10 Molecular Pharmacology and Therapeutics Graduate Program, University of Minnesota Twin Cities, Minneapolis, MN 55455, USA
- 11 Molecular, Cellular, Developmental Biology, and Genetics Graduate Program, University of Minnesota Twin Cities, USA
- 12 Instituto Biofisika CSIC-UPV/EHU, Leioa, Bizkaia, Spain

Correspondence to Louis M. Mansky and Wei Zhang: mansky@umn.edu (L.M. Mansky), zhangwei@umn.edu (W. Zhang)@BioChemTalledge ♥ (N. Talledge), @ManskyVirology ♥ (L.M. Mansky) https://doi.org/10.1016/j.jmb.2023.168143

Edited by Eric O. Freed

#### Abstract

Retrovirus immature particle morphology consists of a membrane enclosed, pleomorphic, spherical and incomplete lattice of Gag hexamers. Previously, we demonstrated that human immunodeficiency virus type 2 (HIV-2) immature particles possess a distinct and extensive Gag lattice morphology. To better understand the nature of the continuously curved hexagonal Gag lattice, we have used the single particle cryo-electron microscopy method to determine the HIV-2 Gag lattice structure for immature virions. The reconstruction map at 5.5 Å resolution revealed a stable, wineglass-shaped Gag hexamer structure with structural features consistent with other lentiviral immature Gag lattice structures. Cryo-electron tomography provided evidence for nearly complete ordered Gag lattice structures in HIV-2 immature particles. We also solved a 1.98 Å resolution crystal structure of the carboxyl-terminal domain (CTD) of the HIV-2 capsid (CA) protein that identified a structured helix 12 supported via an interaction of helix 10 in the absence of the SP1 region of Gag. Residues at the helix 10–12 interface proved critical in maintaining HIV-2 particle

release and infectivity. Taken together, our findings provide the first 3D organization of HIV-2 immature Gag lattice and important insights into both HIV Gag lattice stabilization and virus maturation.

© 2023 Elsevier Ltd. All rights reserved.

### Introduction

Human immunodeficiency virus type 1 (HIV-1) and HIV type 2 (HIV-2) are both etiological agents of acquired immunodeficiency syndrome (AIDS). The HIVs are members of the lentivirus genus of Retroviridae. Relative to that of HIV-1, HIV-2 has an attenuated disease phenotype, with lower viral loads in infected individuals, as well as lower rates of both vertical and sexual transmissibility, and a slower progression to AIDS.<sup>2-7</sup> The HIV-2 genome structure is like that of the HIV-1 genome; however, HIV-2 encodes for vpx instead of vpu.8-10 HIV-1 emerged in the human population via spillover of simian immunodeficiency virus from chimpanzees or gorillas (SIVcpz, SIVgor), while HIV-2 emerged in humans following spillover of SIV from sooty mangabeys (SIVsm). HIV-1 and HIV-2 share approximately 60% amino acid identity between Gag polyproteins and just 48% identity at the viral genome level. 12 As lentiviruses, HIV-1 and HIV-2 mature particles possess similar morphologies that include a conically shaped core structure. 13-14 Immature HIV-1 and HIV-2 particles have been noted to have distinct morphological features. 15

HIV particle assembly is known to occur at the plasma membrane of infected host cells, where multimerization of the Gag structural polyprotein drives the assembly and release of virus particles (for a review, see<sup>16</sup>). The Gag polyprotein consists of three major protein domains: the matrix (MA) domain (which binds membrane), the capsid (CA) domain (which encodes key residues involved in Gag-Gag and CA-CA interactions), and the nucleocapsid (NC) domain (which encodes the key determinants for genomic RNA packaging). 16 HIV-1 and HIV-2 Gag polyproteins both encode for two spacer peptides (i.e., SP1 and SP2) and the p6 domain. During virus maturation, the Gag polyprotein is cleaved by the virally encoded protease to produce the mature viral structural proteins. The emergence of these structural proteins leads to the formation of a conically shaped CA core.

HIV-1 CA is composed of two  $\alpha$ -helical enriched domains connected by a flexible linker. <sup>18–20</sup> The amino-terminal domain (*i.e.*, CA<sub>NTD</sub>) is composed of 7  $\alpha$ -helices (H1 to H7) and includes functional domains that bind to cellular factors such as cyclophilin A (CypA)<sup>18</sup> and TRIM5 $\alpha$ . <sup>21–22</sup> The carboxy-terminal domain (*i.e.*, CA<sub>CTD</sub>) contains 4  $\alpha$ -helices (H8 to H11). The function of the CA<sub>CTD</sub> is primarily to form inter-molecular contacts that are important to the stability of immature Gag lattice and for the

formation of a mature CA lattice that is necessary for particle infectivity.

Multimerization of Gag in immature HIV-1 particles results in hexagonal lattice structure due to extensive interactions among the CA proteins.<sup>23-29</sup> The CA hexamers adopt a wineglass-like structure to accommodate the spherical shape of the viral membrane. The "cup" of the wineglass is composed of six copies of CA<sub>NTD</sub> on the rim and six copies of CA<sub>CTD</sub> at the base of the cup. The "stem" of the wineglass is a six-helix bundle (6HB) structure that consists of the C-terminal tail of CA and the SP1 segment (CA-SP1).30 The CA hexamer in HIV-1 is further stabilized by the cellular metabolite inositol hexakisphosphate (IP6) that is closely positioned within the positively charged rings of lysine residues in the C-terminal end of the CA<sub>CTD</sub> (i.e., Gag residues K290 and K359, or CA residues K158 and K227).30-31 The Gag lattice is stabilized by the molecular interactions of helix 1 and 2 (i.e., H1 and H2) in the CA<sub>NTD</sub> at local two-fold and three-fold axes, respectively, and the CA<sub>CTD</sub> interactions (H9) at the local two-fold axes.30

The HIV-1 capsid core has a fullerene structure composed of approximately 250 CA hexamers and 12 pentamers.  $^{32-38}$  In contrast to the CA hexamers in the immature lattice, each capsomer in the mature CA lattice adopts a bell-shaped structure. The CA\_NTD forms the inner ring and the closed end of the bell. The CA\_CTD forms the outer ring connecting the neighboring capsomers. The HIV-1 CA\_CTD H10 forms the trimer interface and H9 forms the dimer interface between the adjacent CA molecules.

Limited structural details are available for the HIV-2 Gag protein, with the crystal structure of the HIV-2 CA<sub>NTD</sub> being the only high-resolution protein structure of HIV-2 CA solved to date (PDB ID: 2WLV).<sup>39</sup> A previous comparative analysis of immature retrovirus particle morphologies by cryo-electron microscopy (cryo-EM) revealed that HIV-2 immature particles possessed distinct differences from that of HIV-1 or other immature retrovirus particles analyzed. 15 In contrast to what was observed for HIV-1, immature HIV-2 particles had a relatively narrow range of particle diameters and possessed nearly complete Gag lattice structures as assessed by gualitative measurements of the particle morphology. However, to date, no high-resolution structure of immature particles has been analyzed for HIV-2.

To help address this knowledge gap, and to help define the basis for the morphological differences between HIV-1 and HIV-2, we conducted cryo-EM and cryo-electron tomography (cryo-ET) of HIV-2 particles and confirmed that HIV-2 immature

particles have a high occupancy of immature Gag lattice underneath the viral membrane. We determined the HIV-2 Gag hexamer structure at 5.5 Å resolution by using a cryo-EM single particle reconstruction (SPR) method 40. Furthermore, we also solved a 1.98 Å crystal structure of the HIV-2 CA<sub>CTD</sub>, which revealed a novel, extended 3<sub>10</sub> helix at the CTD of CA (H12). Residues that are involved in H10 and H12 interactions in the crystal dimer were found to be critical for maintaining HIV-2 particle infectivity. Taken together, our observations demonstrate - for the first time - that the HIV-2 Gag lattice possesses few interspersed gaps relative to that of HIV-1,<sup>24</sup> with novel findings of critical amino acid residues within the HIV-2 CA<sub>CTD</sub> that are required for infectious particle production. These findings provide insights into the morphological differences observed between HIV-1 and HIV-2 immature particles, as well as general implications for HIV Gag lattice stabilization and virus maturation.

#### Results

## Cryo-EM reconstruction of the immature HIV-2 Gag lattice

We computed the reconstruction map of HIV-2 Gag lattice by using a cryo-EM SPR method

(Figure 1(A), S1). The boxed particle centers are located at the center of the lattice region of the imaged immature particles. These boxed images represent the side views of the segmented Gag lattice. allowing for rapid analysis heterogeneous sized viral particles. Using the sixfold rotational symmetry from the Gag hexamer we computed a reconstruction of the underlying capsid lattice (Figure 1(B-D)). The reconstruction of the HIV-2 CA lattice in immature particles was resolved to 5.5 Å resolution that contains 19 hexamer units of the HIV-2 Gag lattice (Figure 1(C-D), S2).

# Crystal structure of HIV-2 CA<sub>CTD</sub> has a distinct C-terminal 3<sub>10</sub> helix

To help elucidate the molecular basis of the HIV-2 Gag lattice interactions, we expressed and purified the CA CTD residues 145–230 (HIV-2 CA<sub>CTD</sub>, Gag residues T280 to M365) to homogeneity for structure determination. HIV-2 ROD CA<sub>CTD</sub> shares 69% sequence identity with that of HIV-1 NL4-3. This subdomain of HIV-2 CA structure has not been previously reported. The purified protein was crystallized, and the structure determined to 1.98 Å resolution (Figure 2, Table S1). The crystal belonged to the space group C2, with a monomer

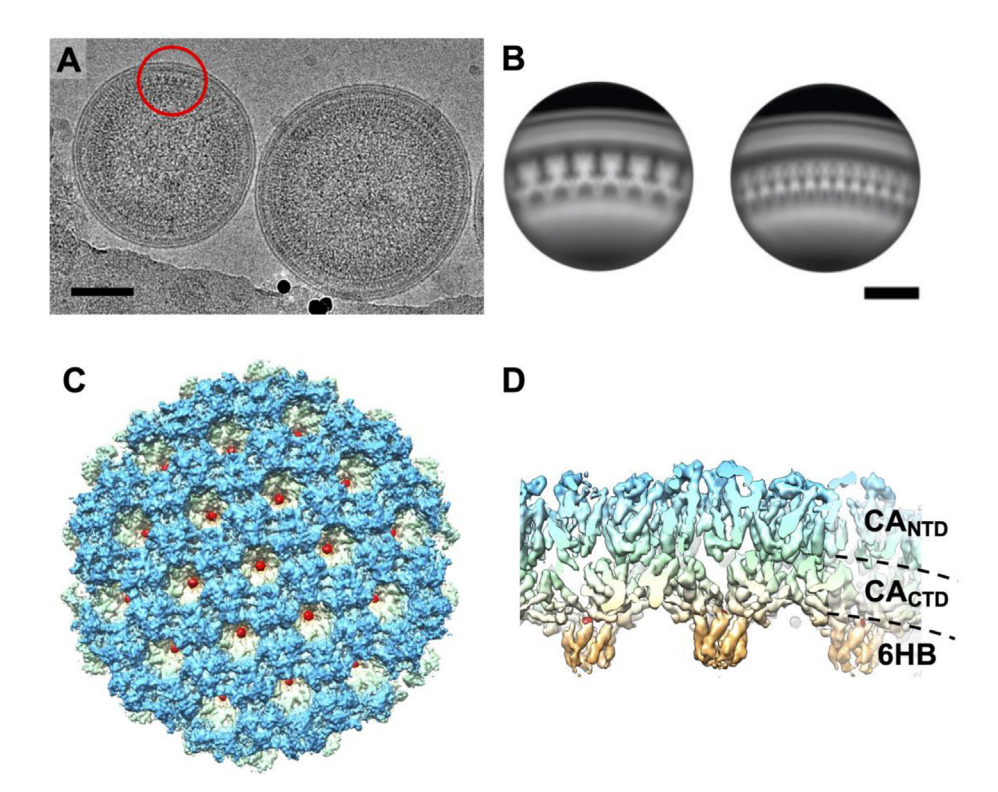


**Figure 1. HIV-2 Gag lattice structure.** (A) Cryo-EM micrograph of immature HIV-2 particles. The red circle indicates an example area of extracted particles for the single particle reconstruction procedure. (B) Representative 2D class averages of the resulting particle extraction at the tangent of the immature HIV-2 particles. The scale bars represent 50 nm. (C)Top and (D) side views of the 5.5 Å reconstruction map showing densities of CA<sub>NTD</sub> (blue), CA<sub>CTD</sub> (light green and yellow), CA-SP1 six helix bundle (6HB, orange), and IP6 (red).

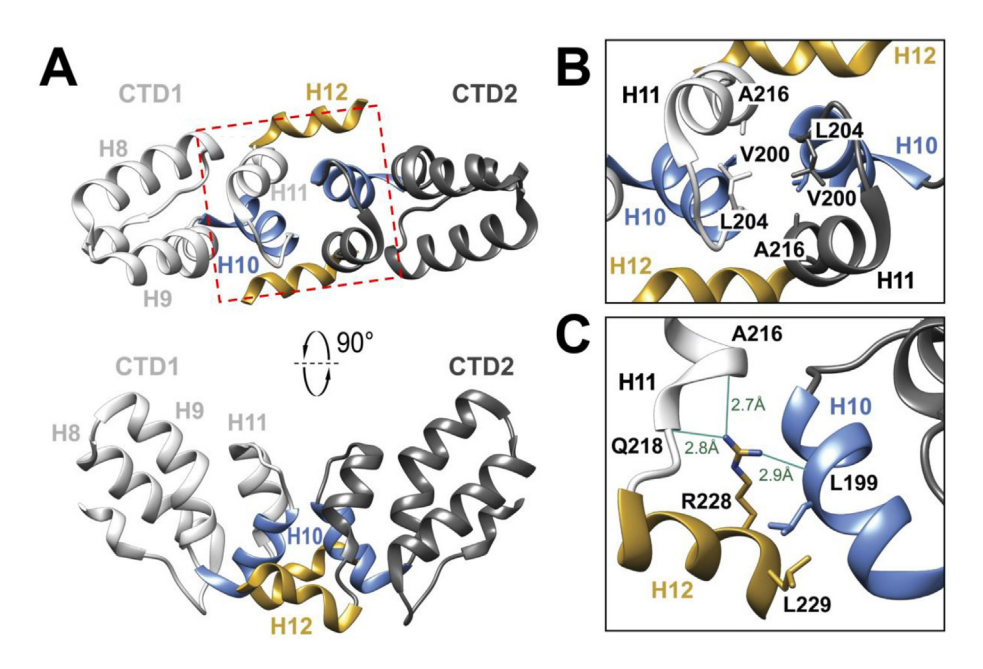


**Figure 2. HIV-2 CA<sub>CTD</sub> crystal Structure.** (A) The structure of HIV-2 CA<sub>CTD</sub> dimer from CA residues T147-M230. H8, H9, H10, and H11 represent the four  $\alpha$ -helices in HIV-2 CA<sub>CTD</sub>. H12 is a 3<sub>10</sub> helix at the C-terminus of the molecule. CTD1 and CTD2 represent two molecules in the dimer. The red box marks the H10-H11 dimer interface which is delineated in B. (B) Magnified view of the H10-H11 crystallographic dimer interface highlighting the residues V200, L204, and A216. (C) Residues L199, R228, and L229 are located at the HIV-2 CA<sub>CTD</sub> H10-H12 crystallographic dimer interface. The guanidinium group of CTD2-R228 forms hydrogen bonds with the backbone oxygen atoms of CTD1-L199, CTD2-A216, and CTD2-Q218.

of HIV-2  $CA_{CTD}$  in the asymmetric unit. Two HIV-2  $CA_{CTD}$  molecules form a symmetric dimer with the 2-fold axis coinciding with the crystallographic dyad. We were able to model CA residues T147 to M230 (Gag residues T282 to M365).

Like that of other lentiviral  $CA_{CTD}$  domains, <sup>39–43</sup> the HIV-2  $CA_{CTD}$  is primarily  $\alpha$ -helical. Furthermore, its tertiary structures (helix 11, H11, and its upstream domain) superimpose with that HIV-1  $CA_{CTD}$  (PDB ID: 1A43) <sup>43</sup> with backbone RMSD of 0.74 Å. The residues downstream of H11 form an extended C-terminal 3<sub>10</sub> helix (referred to as helix 12, or H12).

The HIV-2 CA<sub>CTD</sub> dimer interface involves H10 in one monomer contacting with H10, H11 and H12 in another monomer (Figure 2(B-C)). In contrast, the crystallographic CTD dimer interface in HIV-1 CA<sub>CTD</sub> is composed of the intermolecular interactions between H9 of each monomer. 43 Specifically, the unique HIV-2 CA<sub>CTD</sub> dimeric interface is supported by hydrogen bonds with the backbone oxygen atoms of CTD1-L199 (H10), CTD2-A216 (H11), CTD2-Q218 (H11) and the guanidinium group of CTD2-R228 (H12) (Figure 2(C)). The interface mediated by intermolecular contacts between H10 and H12 contrasts with other retroviruses CA<sub>CTD</sub> as this portion of the CTD is disordered in the absence of the SP1 peptide in other retroviral CA<sub>CTD</sub> structures. 39,43

## The HIV-2 hexagonal Gag lattice resembles that observed in HIV-1

The 5.5 Å reconstruction map of the immature HIV-2 Gag lattice allowed for modeling of the Gag residues S150 to I373 (CA residues S15 to M230 and SP1 residues A1 to I8) into the electron density (Figure 3). The overall molecular fitting of structure indicates a similar structural conformation to that of HIV-1. For example, six copies of the CA and SP1 domains are organized into a wineglass-shaped structure, with CA proteins representing the cup and the CA-SP1 6HB representing the stem (Figure 3(A-B)). The NTD and CTD domains of the HIV-2 CA twist in a left-hand manner, while the 6HB twists in a righthand manner (Figure 3(C)). The length of the 6HB density layers is  $\sim$  25 Å, which can accommodate the predicted 16 amino acid residues of the CA-SP1 region (i.e., Gag residues P358 to I373). The extra globular-shaped densities observed at the top of the 6HB are attributable to IP6 (Figure 3(A-B)). This observation is consistent with what has been previously reported for the HIV-1 immature Gag lattice structure 30,44, and is consistent with the finding that IP6 plays a role in HIV-2 immature particle assembly. 31 Like HIV-1, the HIV-2 Gag inter-hexamer interface is also maintained by the molecular contact regions at both the two-fold and three-fold symmetric axes (Figure 3(D-F)). A num-

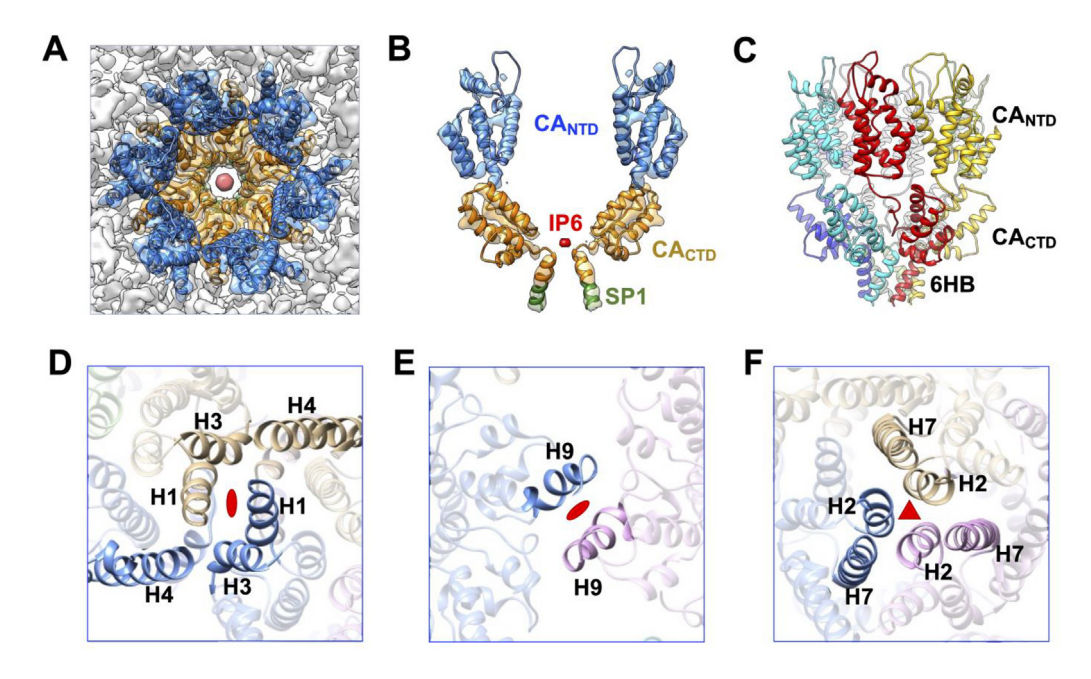


Figure 3. Model of HIV-2 CA hexamer and lattice interfaces. (A) Top view of the central hexamer reconstruction density fitted with the HIV-2 CA model (PDB ID: 8FZC). Blue:  $CA_{NTD}$ ; Orange:  $CA_{CTD}$ ; Red: IP6. (B) Side view of two capsid monomers zoned out of the central hexamer. Green: SP1. (C) Side view of HIV-2 hexamer model color coded by the CA proteins. The depiction shows the left-hand twist of the CA proteins and the right-hand twist of the six-helix bundle (6HB) formed by CA-SP1. (D) View of the NTD two-fold interface in the Gag lattice involving H1. (E) View of the CTD two-fold interface formed by H9. (F) View of the NTD three-fold interface formed by H2.

ber of amino acid residues at the interaction interface are conserved between HIV-1 and HIV-2. For example, the HIV-2 CA H9 residues CA W183 and M184 (Gag residues W318 and M319) are located at the two-fold interface of the Gag lattice. Such structural similarity among lentiviruses indicates the conserved stability of the Gag hexamer as a structural building block of the immature Gag lattice.

## Mutations of H10 and H12 residues decrease HIV-2 particle infectivity

To determine if the extended HIV-2 H12 revealed in the crystal structure has an impact on steps of the retroviral life cycle we made disruptive mutations at critical residues at the HIV-2 CA<sub>CTD</sub> H10 and H12 crystal interface (Figure 4, Figure S7). Specifically, residues L199, R228, and L229 observed at the CA<sub>CTD</sub> crystal structure interface (Figure 2(C)) were mutated to introduce either modest disruptions (L199G, R228A, and L229G) or strong disruptions (L199K, R228E, and L229K). To assess particle assembly defects, we analyzed particle production from expressing a codonoptimized HIV-2 Gag construct harboring the individual mutations in HEK293T/17 cells. Viral supernatants were assessed via immunoblot for the relative amount of Gag present to WT HIV-2 Gag (Figure 4(A); Figure S9). Two mutation sites in H12, i.e., R228 and L229, showed a significant

decrease in produced immature particles, where the H10 L199G and L199K point mutations showed no significance difference to that of WT Gag levels.

To determine if these mutations influenced mature particle morphology, an HIV-2 ROD10-based vector (*i.e.*, an *env*-minus HIV-2 vector containing the mCherry-IRES-GFP reporter gene expression cassette) was co-expressed with VSV-G to produce single-cycle mature infectious particles in HEK293T/17 cells. These particles were used to assess mature particle production and morphology (Figure 4(B); Figure S10). All of the H12 mutations significantly decreased (i.e.,  $\sim\!10$  fold) particle production compared to that of WT. The H10 mutation led to a significant decrease for the L199G (i.e.,  $\sim\!60\%$  that of WT), but the L199K mutation showed no significant difference (Figure 4(B); Figure S10).

The HIV-2 vector virus particles that harbor dual fluorescent reporters were then used to assess particle infectivity by infecting MAGI cells with equivalent amounts of virus as assessed by CA levels in the produced viral supernatant (Figure 4 (B); Figure S10). Specifically, the H10 or H12 mutants harboring particles showed significant defects in infectivity as compared to a WT infection. Particle production was  $\sim$  10 to 20-fold lower to that of WT HIV-2 particles (Figure 4(C)).

Two patterns emerged when assessing mature particle production (Figure 4(B); Figure S10) and

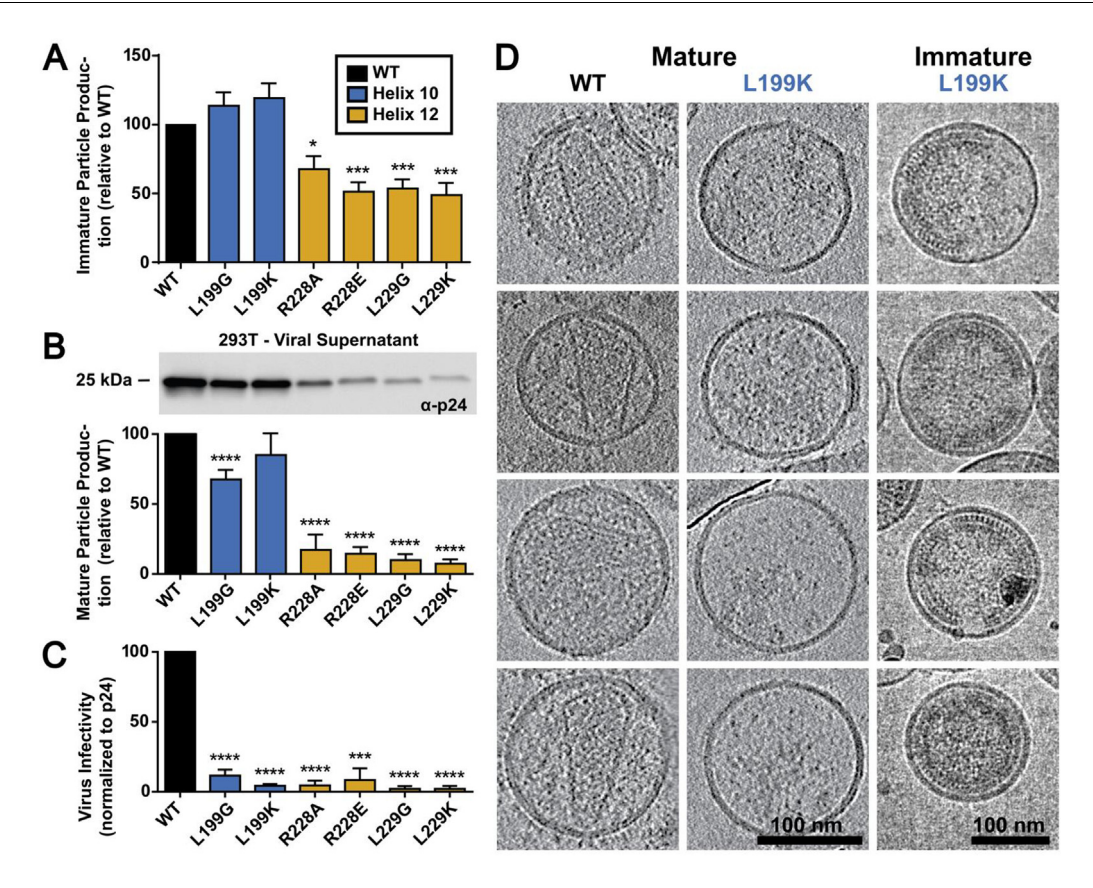


Figure 4. Analysis of mutations in HIV-2  $CA_{CTD}$  H10 and H12 on particle production and infectivity. (A) The effect of H10 and H12 mutations on immature particle production, (B) mature particle production including an immunoblot of the relative levels of CA (p24) present in the viral supernatant, and (C) on particle infectivity is shown. Results are from three independent experiments: average value  $\pm$  standard error of the mean shown. Significance relative to WT as assessed by using an unpaired t-test. \*\*\*\*, P < 0.0001; \*\*\*, P < 0.001; \*\*, P < 0.01; \*, P < 0.05. (D) Morphology of mature and immature HIV-2 WT and L199K mutant particles. The left and the middle columns are representative slices of cryo-ET reconstructions of the HIV-2 MIG vector, and its mutant (L199K). The right column shows cryo-EM images of the immature particles for the L199K mutant.

particle infectivity (Figure 4(C)) for the HIV-2 H10/ H12 mutants. The H12 mutants all led to severe defects in particle production and infectivity. Intriguingly, mutation of the L199 position in H10 retained efficient particle production, significantly reduced particle infectivity. immature and mature HIV-2 CA L199K particles were visualized by cryo-ET to assess particle morphology (Figure 4(D)). HIV-2 WT particles had a canonical mature core morphology with the presence of a fullerene cone in a subset of the produced particles. The HIV-2 L199K immature particles had intact and extensive Gag lattice below the viral membrane, but the L199K mutant had no particles with intact capsid cores, indicating a defect in mature particle formation. To rule out the possibility that mutations in CA impacted the recognition by anti-CA antibodies, a control immunoblot was done in which anti-MA antibodies were used for Gag detection. Immature particle production observed with the anti-MA antibodies (Figure S11) was comparable to that observed with the anti-CA antibodies (Figure S9).

# Cryo-ET reveals high Gag occupancy and minimal gaps in the HIV-2 Gag lattice

The SPR map of immature HIV-2 particles revealed an ordered Gag lattice morphology that occupies an extensively large region underneath the viral membrane, consistent with our group's previous reports when analyzing the cryo-EM images. To fully characterize this observation, cryo-ET was conducted on immature HIV-2 particles purified from HEK 293 T/17 cells. Five cryo-ET tilt series of HIV-2 immature particles were reconstructed in IMOD. Then subtomogram averaging (StA) workflows were implemented in Dynamo followed by RELION-4.0 (Figure 5, S3). 45-47

Gag hexamer lattice positioning was determined in Dynamo by an iterative convolution procedure that correlates the sub-volumes cropped from the IMOD reconstruction maps at regions corresponding to the Gag lattice with the StA averaged map centered at the Gag hexamer model (Figure 5(A)). The calculated HIV-2 Gag hexamer positions within the viral particles were

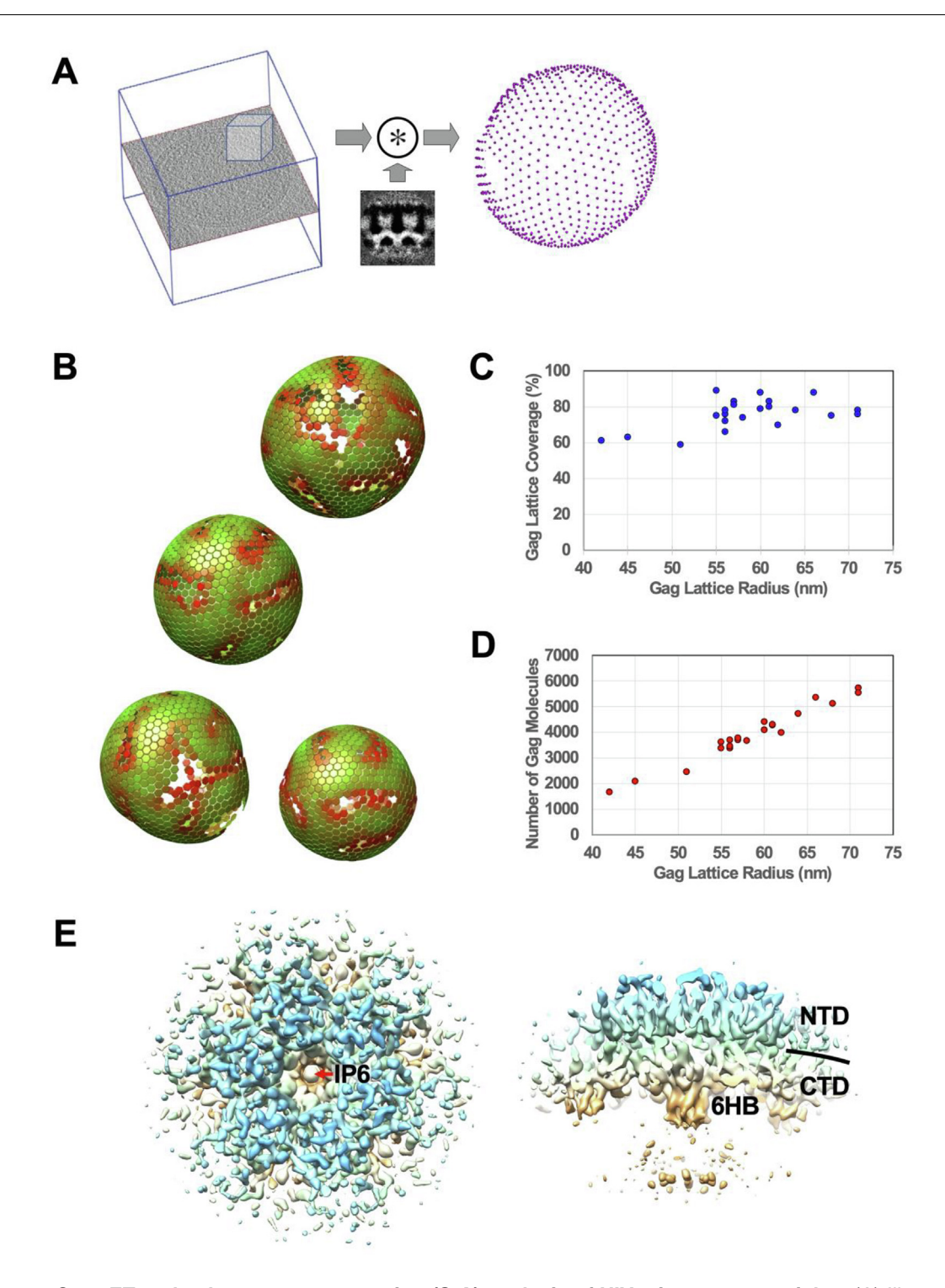
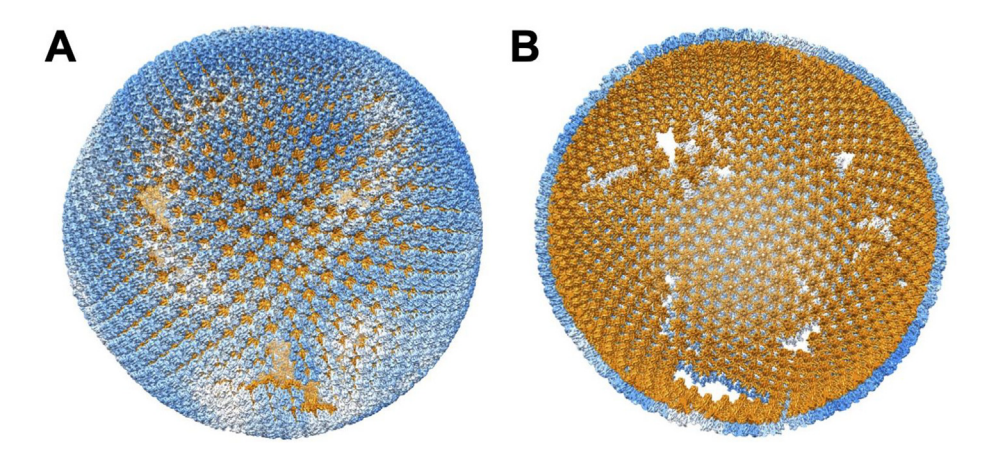


Figure 5. Cryo-ET and subtomogram averaging (StA) analysis of HIV-2 immature particles. (A) Illustration of convolution calculation between a region cropped from a particle (left) with the StA average of the Gag hexamer (middle). The calculation produces the Gag hexamer localizations (right). (B) A graphical depiction of the hexagonal Gag lattices, determined by Dynamo, for four HIV-2 immature particles within the same tomogram. The color denotes how well that hexamer matches with the StA model, with green having a higher correlation coefficient score than red (range: 0.0913 to 0.3592). (C) Gag lattice coverage sorted by the estimated Gag lattice radius per particle. The radius of the Gag lattice is defined as the radius of the linker region (between CA<sub>NTD</sub> and CA<sub>CTD</sub>) of the CA density layer. (D) Estimate of the total number of Gag molecules underneath the viral membrane sorted by the estimated Gag lattice radius per particle. (E) The top and side 3D rendering views of the StA average of a Gag hexamer at 9.1 Å resolution. IP6: inositol hexakisphosphate; 6HB: six helix bundle; NTD: CA<sub>NTD</sub>; CTD: CA<sub>CTD</sub>.



**Figure 6.** A model of HIV-2 immature Gag lattice structure. The model was generated by placing the 5.5 Å CA density onto the Gag lattice determined by Dynamo. (A) Exterior of the HIV-2 CA organization in the Gag lattice. Blue represents the NTD of the CA proteins. White indicates the interspersed gaps of the lattice. (B) Interior of the HIV-2 CA organization. Orange represents the CA<sub>CTD</sub> and the CA-SP1 domains. The figure was produced using the UCSF Chimera<sup>71</sup> plug-in, Place Object.  $^{52}$ 

found to have an almost complete hexagonal lattice pattern with small, interspersed gaps or crevice regions indicated by low positional crosscorrelations from our analysis (Figure 5(B-C), Figure 6, Movie S1). Calculation of the Gag lattice coverage from twenty-five HIV-2 immature particles revealed that the Gag coverage area underneath the viral membrane was as high as  $\sim$  90% (Figure 5(C), S5, Table S3), with the average membrane coverage ratio being 76 +/-8%. The number of Gag molecules in the Gag lattice of these particles ranges from  $\sim$  1700 to  $\sim$  5700, with the average being  $\sim$  3900 +/-1000 (Figure 5(D), Table S3). The StA average of the Gag hexamer was carried out on ordered Gag hexamer positions by Dynamo<sup>45,46</sup> and RELION-4.0<sup>47</sup> (Figure S3). The final reconstruction map (Figure 5(E), S4) at 9.1 Å resolution revealed consistent structural features shown in the 5.5 Å map (Figure 1) that were computed by using the SPR method.

To validate the observation of the Gag lattice was not due to the Gag expression system, we generated authentic immature HIV-2 particles (Figure S6). To do this, critical residues in the catalytic domain of the HIV-2 protease (PR) were mutated (i.e., D25N/T26A/E37K)<sup>48</sup> in a HIV-2 ROD10 infectious molecular clone, and this was used to transiently transfect HEK293T/17 cells in order to generate authentic, non-infectious HIV-2 immature particles. Immunoblot analysis was performed on the released particles to confirm that no Gag processing had occurred, which was interpreted as indicating that the viral protease had been inactivated (Figure S6(A)). Cryo-EM analysis of these particles confirmed that authentic, immature HIV-2 particles could also possess an intact and near complete immature CA lattice (Figure S6(B)).

### **Discussion**

A previous study utilized a parallel comparative analvsis investigate immature particle to morphologies among viruses representing the various retroviral genera. 15 Notably, it was observed that there were differences in the general subcellular distribution of the various retroviral Gag proteins as well as their being differences in the general morphology of the released immature particles. Furthermore, differences were observed among both the Orthoretrovirinae as well as the representative member of the Spumaretrovirinae. Intriguingly, among the observations made was that HIV-2 immature particles possessed a narrow range of particle size and had consistent regularly distributed electron density below the viral membrane, suggesting a tightly packed Gag lattice - in contrast to what was observed with HIV-1 immature particles. The use of crvo-ET and StA allowed for determination that the Gag lattice coverage in HIV-2 immature could be as high as  $\sim 90\%$  (Figure 5(C), 6), in contrast to HIV-1 in which Gag lattice covers about 60% of the viral membrane. 49,50 The differences in HIV-1 and HIV-2 pathogenicity provide the impetus for gaining deeper insights into the biological differences of these closely related lentiviruses, particularly in gaining new insights into retroviral assembly.

We used cryo-EM SPR to solve the immature HIV-2 Gag hexamer structure at 5.5 Å resolution. Fitting of HIV-2 CA<sub>NTD</sub> and CA<sub>CTD</sub> structures into the resolved density map demonstrated a wineglass-like architecture of the central hexamer that is very reminiscent to that of HIV-1,<sup>30</sup> equine infectious anemia virus (EIAV)<sup>51</sup> and murine leukemia virus (MLV).<sup>52</sup> The HIV-2 Gag hexamer was found to be stabilized by conserved residues in H2

at the three-fold inter-hexamer interface, by H9 in the CA<sub>CTD</sub> at the two-fold inter-hexamer interface. and by a 6HB formed by the CA-SP1 at the sixfold intra-hexamer interface. We also observed a strong central pore density between the base of the CA<sub>CTD</sub> and the 6HB that is consistent with the structural co-factor IP6. The observation of density in the central pore that likely represents IP6 is consistent with observations from previously determined retroviral structures. 31,53,53 The role of IP6 in CA-CA and Gag-Gag self-assembly was predicted by the pioneering studies conducted by Rein and coworkers.<sup>54</sup> For HIV-2, it is known to contain conserved lysine residues found within two rings of six lysine residues at the C-terminal end of CA<sub>CTD</sub> (K157 and K226, or Gag residues K292 and K361, in HIV-2).51,53,55

Amino acid variation between the HIV-1 and HIV-2 CA proteins (i.e.,  $\sim$ 70% sequence identity) imply that subtle differences in the structural configuration of their Gag hexamer and lattice organization can have important implications for virus structure and particle infectivity. For example, at the Gag lattice three-fold interface, we found that exchanging HIV-1 and HIV-2 residues significantly reduced virus particle production, and diminished virus particle infectivity. Mutations of a non-conserved residue in helix 2 of the CA proteins - i.e., HIV-2 CA G38M and HIV-1 CA M39G - reduced by 50% virus particle production as well as eliminating virus infectivity.<sup>56</sup> Additionally, the HIV-2 CA N127E mutant, which introduced the HIV-1 encoding residue into HIV-2 CA, severely reduced particle production. It should be further noted that HIV-2 is insensitive to the HIV-1 maturation inhibitor bevirimat (BVM), 57-59 emphasizing that subtle differences in structural properties between the HIV-1 and HIV-2 Gag proteins can have important implications in retrovirus replication. The binding site of BVM has been determined to be inside the CA-SP1 six-helix bundle near the IP6 binding site. 30,59,60 Taken together, these observations argue for the importance in obtaining a near-atomic structure of HIV-2 immature Gag lattice to gain further mechanistic insights into the comparative differences between HIV-1 and HIV-2 CA structure.

From the HIV-2 CA<sub>CTD</sub> crystal structure, it can be inferred that residues in H10 and H12 play a critical role in mediating the dimeric interface in the crystal. In particular, the C-terminal residues of the HIV-2 CA form a 3<sub>10</sub> helix, *i.e.*, H12. The angle in which the HIV-2 CA<sub>CTD</sub> H12 extends from H11 is different from that in our immature HIV-2 CA lattice from particles (Figure S7(A-B)), as well as immature HIV-1 CA-SP1 lattice from in vitro assemblies or virus particles.<sup>30</sup> However, modeling of the HIV-2 CA<sub>CTD</sub> crystal structure into the HIV-1 mature CA capsid implies that the putative H12 is in the vicinity of H10 in the adjacent hexamer at the three-fold CA inter-hexamer interface (Figure S7(C-D)). Therefore, additional studies were

conducted to assess the biological relevance of the residues in these helices.

Site-directed mutagenesis of the HIV-2 CA L199 (in H10), along with R228, and L229 (in H12) led to severe impairments in particle production and infectivity (Figure 4(A-C)). This implies that the residues at the H10 and H12 revealed in the HIV-2 CA<sub>CTD</sub> crystal may be important for HIV-2 morphology and particle infectivity, and help explain the morphological features distinct from that of HIV-1.

Cryo-EM micrographs (Figure 4(D), S8) show that mutations at a H10 residue L199 (L199K and L199G) did not significantly change particle production in the immature particles and immature Gag lattice features were prevalent within the particles. No capsid cores were observed in the mature particles for the L199K mutant. For L199G, less than two percent of observed particles have internal densities that are attributable to the presence of a full or partial capsid core. However, the mutant is not infectious suggesting these cores are defective. Mutation at the H12 residue R228 (i.e., R228E) did not eliminate Gag assembly. But the Gag densities in R228E immature particles appear different from the normal Gag lattice in the WT HIV-1 and HIV-2 immature particles. Intriguingly, these lattice-like densities resemble the morphology of HIV-1-CA<sub>NTD</sub>/HTLV-1-CA<sub>CTD</sub> chimera particles that we previously reported using similar analyses. 61 No capsid cores were observed in mature R228E particles. Presumably, this is because the HIV-2 CA residues R228 and L229 are part of the 6HB and are 3 and 2 amino acids upstream of the CA-SP cleavage site (i.e., CA M230 and SP1 A1, respectively), it is possible that mutations at these residues impair proper Gag assembly and protease cleavage, thus preventing the formation of the mature CA lattice. Nevertheless, the phenotypes of mutations on the H10 residue L199 are clearly novel and not postulated by the current lentivirus CA structural model. For example, the aligned residue of HIV-2 L199 in HIV-1 H10 (i.e., T200) is not directly involved in any molecular interaction in either immature Gag (e.g., PDB ID: 5L93) or mature CA lattice structures (e.g., PDB ID: 5MCX and 6SKN). Determination of the high-resolution structure of mature HIV-2 CA lattice and understanding the implications of the mutagenesis studies on HIV-2 replication and on the mechanistic basis of HIV-2 maturation represent an important area for future studies.

### **Materials and Methods**

## HIV-2 CA<sub>CTD</sub> protein purification, crystallization, and structure determination

We expressed HIV-2  $CA_{CTD}$  (residues 145–230) in *E. coli* strain BL21 (DE3) with a N-terminal 6xHis-tag, using the pET28a expression vector. The expressed protein was purified by Ni-NTA affinity and Superdex 75 size-exclusion chromatography (SEC) steps. The  $6 \times His$ -tag was

removed by a treatment with HRV 3C protease after elution from the Ni-NTA column and prior to the SEC step. The purified protein in 20 mM Tris-HCl (pH 7.4), 0.5 M NaCl, + 5 mM  $\beta$ -mercaptoethanol was concentrated by ultrafiltration to  $\sim$  43 mg/ml. Crystallization screening was performed on a Phoenix (Art Robbins Instruments, USA) crystallization robot. Crystals appeared in one day and grew to full size in three days. The crystals that gave the best diffraction were grown under the condition of 1.2 M tri-sodium citrate, 0.1 M Bis-Tris propane, pH 7.0.

The HIV-2 CA<sub>CTD</sub> crystals were cryo-protected by soaking in the crystallization reservoir solution supplemented with 25% ethylene glycol and flash cooled in liquid nitrogen. X-ray diffraction data were collected at the 24-ID-E beam line of the Advanced Photon Source, using the wavelength of 0.979 Å and processed using HKL2000. The crystal structure was solved by the molecular replacement phasing, using the coordinates of the T58A/I124A mutant of the HIV-1 capsid protein (PDB ID: 6AXX) as the search model. Iterative model building and refinement were performed using COOT<sup>62</sup> and PHENIX<sup>32</sup> giving a final Rwork of 22.39% and Rfree of 24.95%. The final model consists of 84 amino acids. Refinement and validation metrics are listed in Table S1.

### Immature particle production and purification

The HIV-2 gag gene (bases 546 to 2114 from GenBank accession number M15390) was used as the basis to create a codon-optimized gag gene that was cloned into the pN3 expression vector that included a 5' Kozak sequence (GCACCATG, start codon in bold). The pN3-gag expression constructs and their homologous (gp160) envelope alvcoprotein expression plasmids were co-transfected into HEK293T/17 or 293F cells using GenJet Ver. II (SignaGen Laboratories, MD) at a mass ratio of 10:1 (Gag: Env). After 48 h (for HEK293T/17 cells) or 120 h (for 293F cells) post-transfection, the cell culture supernatant was harvested and filtered through a 0.22 µm filter. Purification of the particles was conducted by a series of ultracentrifuge steps. Initially, the cell culture supernatant was pelleted over an 8% (v/v) OptiPrep<sup>TM</sup> cushion in STE buffer (100 mM NaCl, 10 mM Tris-Cl pH 7.4, 1 mM EDTA) with a 50.2 Ti rotor (Beckman Coulter, CA) at 35,000 rpm for 90 min. The pellet was resuspended in STE buffer and banded out over an OptiPrep<sup>TM</sup> step gradient (10, 20, 30% OptiPrep<sup>TM</sup> (v/v)) with a SW55 Ti rotor (Beckman Coulter, CA) at 45,000 rpm for 3 h. The banded particle sample was extracted from the gradient and a final pelleting reaction step was conducted with a 40,000 rpm spin for 1 hr, prior to being suspended in STE buffer.

#### Mature particle production

The HIV-2 pROD-MIG plasmid and a VSV-G expression construct were co-transfected into HEK293T/17 cells using GenJet Ver. II (SignaGen Laboratories, MD) at a 3:1 mass ratio to produce WT and mutant infectious viral particles. After 48-hours post-transfection, the cell culture supernatants were harvested. clarified centrifugation (1,800 $\times g$  for 10 min), and filtered through 0.22 µm filters. Then the supernatants were concentrated by ultracentrifugation in a 50.2 Ti rotor (Beckman Coulter, CA) at 35,000 rpm for 90 min through an 8% OptiPrep<sup>TM</sup> (Sigma-Aldrich, MO) cushion. The efficiency of mature particle production was analyzed by quantifying the CA (p24) band in culture supernatants using anti-HIV-1 p24 primary antibodies (NIH HIV Reagent Program, Manassas, VA - Mouse anti p24: ARP-6521) and goat anti mouse IRDye® 800CW (LI-COR Biosciences, NE). Capsid protein levels were assessed by SDS-PAGE followed by immunoblotting with an anti-HIV-1 CA (p24) antibody. CA expression levels were normalized relative to GAPDH levels, and the mutant Gag expression levels were determined relative to that of WT HIV-2 Gag.

### **Authentic HIV-2 particle production**

The HIV-2 ROD10 infectious molecular clone was modified by introducing several mutations in the HIV-2 protease active site (*i.e.*, D25N/T26A/E37K). <sup>48</sup> Particles were produced in HEK293T/17 cells in the same fashion as the mature particles. Cell lysates and cell culture supernatants were collected and immunoblotted for HIV-2 Gag using a p24 antibody to confirm a full-length intact Gag (Figure S6).

## Quantification of Gag and CA proteins in WT and mutant viruses

The Gag or CA protein concentrations of the immature or mature HIV-2 particles were first measured by using the BCA assay (Pierce, Rockford, IL). The samples were subjected to SDS-PAGE and then transferred to nitrocellulose membranes. The Gag and CA proteins from immature or mature particles were detected with a 1:1,500 dilution of mouse anti-HIV p24 antibody (Catalogue #: ARP-6521; NIH HIV Reagent Program, Manassas, VA) in 5% milk TBST (Trisbuffered saline plus Tween-20 (1% v/v)). Membranes were washed before incubation with a anti-mouse 1:5000 IRDve® goat 800CW secondary. To compare the Gag or CA protein quantification of WT to that of mutant, HEK293T/17 cells were collected and lysed with Cellytic™ M cell lysis buffer buffer (Sigma-Aldrich, MO) and clarified via centrifugation (1800 $\times g$  for 10 min). The Gag and CA proteins in cell lysates were detected with a 1:2,000 dilution of mouse

anti-HIV p24 antibody (Catalogue #: ARP-6521; NIH HIV Reagent Program, Manassas, VA) and 1:10,000 rabbit anti-GAPDH antibody (Catalogue ab128915; Abcam, Cambridge, Kingdom) in 5% milk TBST. Membranes were washed before incubation with a 1:5000 dilution of goat anti-mouse IRDye® 800CW and a 1:5000 dilution of goat anti-rabbit IRDye® secondary. The membranes of the immunoblots were imaged by using a ChemiDoc Touch system (Bio-Rad, CA). The densities of the protein bands were measured by using ImageJ. To access particle production (i.e., particle release) of mutants relative to that of WT, the Gag or CA expression levels detected from cell lysates of the WT and mutants were normalized relative to the respective GAPDH level. Mutant particle release to that of WT was determined by the ratio of Gag levels detected from cell culture supernatants to that from the normalized Gag levels from the cell lysate, with WT particle release being set to 100 and particle release of the mutants being relative to that of the WT. Results were plotted by using GraphPad Prism 6.0 (GraphPad Software, Inc., CA). Relative significance between a mutant and WT was determined by using an unpaired t-test. Immunoblot analyses were done in three independent replicates to access either immature particle production (Figure 4(A), Figure S9) or (Figure mature particle production 4(B). Figure S10). To confirm the immunoblot analysis done with anti-CA antibodies was not influenced by the CA mutations, control experiments were done using an anti-HIV-1 p17 antibody (Cat. No. sc-69723, Santa Cruz Biotech, TX) (Figure S11).

### Infectivity assay

The HIV-2 pROD-MIG plasmids and the VSV-G expression construct were co-transfected into HEK293T/17 cells using GenJet, ver II (SignaGen, Gaithersburg, MD) at a 3:1 ratio to produce WT and mutant infectious viral particles. After 48hours post-transfection, the viral supernatants harvested, clarified by centrifugation  $(1.800 \times q \text{ for } 10 \text{ min})$ , and filtered through 0.22 µm filters. U373-MAGI-CXCR4 cells were plated in a 12-well plate and each was treated with 1 ml viral supernatants and 1 mL fresh medium. Each group had 4 well replicates. The cells were collected for fluorescence analysis via BD LSR II flow cytometer (BD Biosciences, NJ) 48-hours postinfection as described before.<sup>55</sup> Flow cytometry data were examined in FlowJo v.7 (Ashland, OR). The infectious cells were calculated from the flow data by adding all positive quadrants (mCherry+ only, GFP+ only, and mCherry+/GFP+) to determine infectivity. Mutant infection level was determined related to WT. Then, the relative infectivity of each group was normalized to its relative mature particle production. Three independent experiments were performed (Figure 4(C)).

## Transmission electron microscopy (TEM) sample preparation

The frozen-hydrated TEM grids are prepared by using a FEI MARK III Vitrobot system. A small volume ( $\sim$ 3.5  $\mu$ I) of concentrated particle sample, or particle mixed with BSA-treated 20 nm Nano gold particles, were applied to a glow-discharged Quantifoil holey carbon grid (Ted Pella, Redding, CA) and then blotted with a filter paper before being plunged into liquid ethane. The frozen grids were first examined and screened in an in-house FEI TF30 field emission gun transmission electron microscope at liquid nitrogen temperature (FEI Company, Hillsboro, OR).

### Single particle data collection and reconstruction

The cryo-EM data used for image processing were collected on a Titan Krios TEM at the National Cryo-EM Facility, Cancer Research Frederick National Technology Program, Laboratory for Cancer Research. The images were recorded using a K2 Summit direct electron detector that was positioned post a Gatan BioQuantum energy filter with a 20 eV energy slit for the zero-loss image collection. The cryo-EM movies were recorded at 105,000× nominal magnification, which corresponds to 0.66 Å at the specimen in super resolution mode. Each movie contains 40 frames with an accumulated electron dose of 30-50  $e^-/\mathring{A}^2$ . The defocus levels for the cryo-EM data collection were set to 0.75 to 2.25 μm. The whole data set contains 2508 movies. Movies were motion corrected and doseweighted using the MotionCor2 program.<sup>63</sup> The contrast transfer function (CTF) parameters were determined using Gctf.<sup>64</sup> Detailed data acquisition parameters are listed in Table S2.

The single particle reconstruction was processed in RELION-3.1 (Figure S1(A)). 65,66 Initially, ~1,000 Gag lattice regions on the edges of the particles were picked out from 2415 micrographs to generate initial 2D averages as templates. Then, 219,321 particles were identified by using a template-based auto picking procedure implemented in RELION-3.1. The box size of these local Gag lattice regions was 400 pixels, corresponding to 528 Å on the specimen. The extracted particles were subjected to multiple cycles of 2D classification (remove contaminates and disordered classes) and 3D classification (identify a homogenous set of particles). The final reconstruction from a selected 46,017 particles.

To conduct the Fourier-shell correlation coefficient (FSC) analysis, a customized routine was developed to sort the particles into two non-overlapping data sets of the roughly equal number of particles according to their locations in the micrographs (Figure S1(B)). Briefly, the particles within each micrograph were first separated into

multiple clusters, with the distance between any two clusters larger than a given threshold. Next, clusters in all micrographs were assigned to one of the two data sets alternatively based on the cluster size, to maintain roughly equal number of particles between the two data sets. The algorithm was implemented in the MATLAB programming language. This method avoids assigning the overlapped regions of the crystalline Gag lattices into the same half data set. The final resolution was determined to be 5.5 Å at the FSC cut-off of 0.143 (Figure S2).

### Gag lattice model building and refinement

The HIV-2 CA-SP1 protein structural model is generated from three components. The NTD (Gag residues:S150 to Y279) from HIV-2 NTD structure (PDB ID: 2WLV), CTD (T282 to C352, the crystal structure), and CA-SP1 (Q353 to I373) from threading the HIV-2 ROD CA sequence over the immature HIV-1 Gag cryo-EM structure (PDB ID: 5L93). The residues N280 and P281 were added manually to complete the sequence. The protein models were generated by performing iterative cycles of the real-space refinement routines in Phenix and manual perturbations in Coot. 62

# Cryo-ET reconstruction and subtomogram averaging

Cryo-ET reconstruction of immature HIV-2 particles, HIV-2 MIG construct, and its mutant was carried out by using IMOD<sup>67</sup> and EMAN2<sup>68</sup> respectively. The microscope defocus levels for the tilt series were determined by CTFFIND4.<sup>69</sup> The CTF corrected reconstruction maps of immature HIV-2 particles were used for further StA analysis. The StA of HIV-2 Gag hexamers of 20 immature particles from five tilt series was carried out by an approach using Dynamo<sup>70</sup> and RELION-4.0<sup>47</sup> (Figure S3).

The StA procedure using Dynamo has been previously described in detail. 45 Briefly, the annotated centers and radii of the particles were used to generate an initial sampling of 12,109 points of all particles. These sampling points are regularly distributed on a sphere of the measured radius of each particle with an average distance of 92 A between closest positions. Subtomograms with a box size of 256 pixels (338 Å) were cropped on the sampling positions and were assigned with initial orientations along the normal direction to the surface of the particle with randomized azimuth angles. The averaged map from the particles within one tilt series was used as the starting model for the initial alignment. The relative orientations and positions of the subtomograms from all tilt series were then calculated using C1 symmetry. The resulting map was then shifted so that the center of the Gag hexamer was aligned with the z axis of the model. The new map was then used as the second model for further

refinement with C6 symmetry. Next, for each particle, a new set of 19 sampling points are generated according to the relative positions of the Gag hexamers in the lattice. The subtomogram data set was expanded to 37,081 subtomograms for the total 20 immature HIV-2 particles. The new set of subtomograms with a box size of 192 pixels (253 Å) were extracted from the IMOD reconstruction maps. Further refinement resulted in a converged map.

A two-step selection procedure was employed to further narrow down the subtomograms prior to refinement by using RELION-4.0. First, a custom MATLAB algorithm was developed to clean up the small amount of data points that were in the membrane envelope. An estimated smooth and robust Gag lattice surface was first generated by multiple cycles of computation that fits each point and its surrounding points to a spherical cone and rejects the outlier point. The statistical distribution of the distance between each data point to the theoretical surface was then used to determine a threshold value that filtered out the spurious outer shell points. A set of particle data points (14,675 points) with the orientation within 15 degrees from the norm of the modeled Gag lattice surface were selected. Next, the UCSF Chimera<sup>71</sup> plug-in routine, Place Object,52 was used to display the Gag lattice points color-coded by the correlation coefficient (CC) values between the sub-volumes with the averaged map (Figure 5(B)). A CC threshold was determined by eye for each tomogram to remove the data points on the edges of the continuous Gag lattice patch resulting in the data set of the ordered lattice regions. This procedure resulted into 10,333 positions that were subjected to further refinement in RELION-4.0. Pseudosubtomograms with a box size of 256 pixels (338 Å) were extracted from the original tilt series. A de novo model was generated and used for calculating the orientations and positions to produce an average map with C6 symmetry. The tomo CTF and frame alignment were carried out in RELION-4.0 and the final reconstruction map was determined to be 9.1 A based on the Fourier Shell correlation cut-off of 0.143 (Figure S4).

### Coverage of Gag molecules underneath the viral membrane

The surface area covered by Gag molecules organized in hexagonal lattice was estimated for each HIV-2 immature virus particle. The dense seed locations of 10 pixels distance (13.2 Å) on generated. lattice the Gag laver were Subtomograms with a box size of 100 pixels (132 Å) cropped from the tomograms at these positions contain at least one Gag hexamer within the box. The resulting 624,669 boxes (from 25 immature HIV-2 particles) were realigned using Dvnamo<sup>46,70</sup> allowing them to shift freely around the surfaces of the particles. After alignment, duplicates of final positions representing the same physical particle were located by DBSCAN<sup>65</sup> removed, producing a clean data set of unique box positions (Figure S5(A)). The distribution pattern of the candidate Gag hexamer centers around each data point was investigated through the "neighborhood analysis" method.37 In this approach, the relative distances and angles were computed for every pair of aligned subtomograms present in the data set, showing that the computed positions for the neighbors of a given Gag hexamer are typically distributed in a local hexagonal lattice with a step of 50 pixels (66 Å). After observing the emergence of a hexagonal pattern, the subtomograms that had at least 4 closest neighbors at the distance imparted by this pattern were kept (Figure S5(B-C)). The total number of Gag molecules involved in formation of the Gag lattice in the immature virus particle is estimated to be six times of the total number of remaining subtomograms, which is also used to compute the percentage of the particle surface covered by the Gag hexamers (Figure S5 (D), Table S3).

#### Accession numbers

The refined model of the HIV-2 C-CTD crystal structure was deposited in the protein data bank (PDB ID: 7TV2). The 5.5 Å cryo-EM SPR map of the HIV-2 Gag lattice, the 9.1 Å cryo-ET/StÅ map, and the hexamer model fitted into the 5.5 Å SPR map have been deposited in the EMDB and PDB with accession codes EMD-29607, EMD-29606, and PDB ID: 8FZC, respectively.

### **Declaration of competing interest**

The authors declare that they have no known competing financial interests or personal relationships that could have appeared to influence the work reported in this paper.

### **Acknowledgements**

This work is supported by NIH grant R01 Al177264 (to L.M. and W.Z.). Support is also acknowledged from NIH grants R35 GM118047 (to H.A.) and R21 Al148328 (to W.Z. and L.M.). D. C.D. acknowledges the support of the grant 205321/179041 of the Swiss National Science Foundation (SNF), the grant RGP0017/2020 of the Human Frontiers Science Program (HFSP), and funding from the project PID2021-127309NB-100 funded by AEI/10.13039/501100011033/ FEDER, UE. This research was, in part, supported by the National Cancer Institute's National Cryo-EM Facility at the Frederick National Laboratory for Cancer Research under contract HSSN261200800001E. Parts of this work were carried out in the Characterization Facility, University of Minnesota, which receives partial support from the NSF through the MRSEC (Award Number DMR-2011401) and the NNCI (Award Number ECCS-2025124) programs. Cryo-ET data collection of HIV-2 MIG construct, and mutants were carried out by Dr. Xiaofeng Fu at the Biological Science Imaging Resource at Florida State University through the U24 GM116788 program. X-ray diffraction data were collected at the Northeastern Collaborative Access Team beamlines, which are funded by NIH (NIGMS P30 GM124165). Cryo-ET StA computations were carried out on the GPU clusters at Minnesota Supercomputing Institute. N.T. was supported by NIH grants T32 DA007097, F32 Al150351, and American Cancer Society Postdoctoral Fellowship PF-21-189-01-MPC. W.G.A. was supported by the Institute for Molecular Virology Training Program (i.e., NIH grant T32 Al83196).

#### **Author contributions**

L.M. and W.Z. designed the research. N.T. and L. M. Mendonca purified the immature HIV-2 particles. performed cryo-EM N.T. and crvo-ET reconstructions. K.S. and H.A. solved the crystal structure of HIV-2 CA<sub>CTD</sub>. H.Y., S.M. and W.G.A., performed mutagenesis studies. H.Y. and G.C.B. analyzed production and performed infectivity assays of HIV-2 WT and mutant viruses. H.Y. and S.M. produced mutant viruses for cryo-EM examination. N.T. and W.Z. imaged the WT and mutant virus samples by cryo-EM. W.Z., R.C. and D.C.D. analyzed the Gag lattice structure by the cryo-ET StA method. R.C. and D.C.D. computed the surface coverage of Gag lattices using the DBSCAN and neighborhood analysis methods. G.Y. wrote several imaging processing and analysis programs that enhanced quality and efficiency of the computation. N.T. and K.S. performed structural modeling and fitting. All authors contributed to either drafting and/or revising the paper.

### Appendix A. Supplementary data

Supplementary data to this article can be found online at https://doi.org/10.1016/j.jmb.2023.168143.

Received 2 September 2022; Accepted 1 May 2023; Available online 6 May 2023

Keywords:
retrovirus;
lentivirus;
morphology;
cryo-electron microscopy;
virus assembly

<sup>†</sup> Contributed equally to this paper.

### References

- Nyamweya, S., Hegedus, A., Jaye, A., Rowland-Jones, S., Flanagan, K.L., Macallan, D.C., (2013). Comparing HIV-1 and HIV-2 infection: Lessons for viral immunopathogenesis. Rev. Med. Virol. 23, 221–240.
- Adjorlolo-Johnson, G., De Cock, K.M., Ekpini, E., Vetter, K. M., Sibailly, T., Brattegaard, K., et al., (1994). Prospective comparison of mother-to-child transmission of HIV-1 and HIV-2 in Abidjan. *Ivory Coast. JAMA*. 272, 462–466.
- Andersson, S., Norrgren, H., da Silva, Z., Biague, A., Bamba, S., Kwok, S., et al., (2000). Plasma viral load in HIV-1 and HIV-2 singly and dually infected individuals in Guinea-Bissau, West Africa: significantly lower plasma virus set point in HIV-2 infection than in HIV-1 infection. *Arch. Intern. Med.* 160, 3286–3293.
- Kanki, P.J., Travers, K.U., S, M.B., Hsieh, C.C., Marlink, R. G., Gueye, N.A., et al., (1994). Slower heterosexual spread of HIV-2 than HIV-1. *Lancet* 343, 943–946.
- Marlink, R., Kanki, P., Thior, I., Travers, K., Eisen, G., Siby, T., et al., (1994). Reduced rate of disease development after HIV-2 infection as compared to HIV-1. Science 265, 1587–1590.
- O'Donovan, D., Ariyoshi, K., Milligan, P., Ota, M., Yamuah, L., Sarge-Njie, R., et al., (2000). Maternal plasma viral RNA levels determine marked differences in mother-to-child transmission rates of HIV-1 and HIV-2 in The Gambia. MRC/Gambia Government/University College London Medical School working group on mother-child transmission of HIV. AIDS 14, 441–448.
- Popper, S.J., Sarr, A.D., Travers, K.U., Guèye-Ndiaye, A., Mboup, S., Essex, M.E., et al., (1999). Lower human immunodeficiency virus (HIV) type 2 viral load reflects the difference in pathogenicity of HIV-1 and HIV-2. *J Infect Dis* 180, 1116–1121.
- Hu, W., Vander Heyden, N., Ratner, L., (1989). Analysis of the function of viral protein X (VPX) of HIV-2. *Virology* 173, 624–630.
- Rucker, E., Grivel, J.C., Munch, J., Kirchhoff, F., Margolis, L., (2004). Vpr and Vpu are important for efficient human immunodeficiency virus type 1 replication and CD4+ T-cell depletion in human lymphoid tissue ex vivo. *J. Virol.* 78, 12689–12693.
- Strebel, K., Klimkait, T., Maldarelli, F., Martin, M.A., (1989).
   Molecular and biochemical analyses of human immunodeficiency virus type 1 vpu protein. *J. Virol.* 63, 3784–3791.
- 11. Tebit, D.M., Arts, E.J., (2011). Tracking a century of global expansion and evolution of HIV to drive understanding and to combat disease. *Lancet Infect. Dis.* 11, 45–56.
- Dilley, K.A., Ni, N., Nikolaitchik, O.A., Chen, J., Galli, A., Hu, W.S., (2011). Determining the frequency and mechanisms of HIV-1 and HIV-2 RNA copackaging by single-virion analysis. *J. Virol.* 85, 10499–10508.
- Goto, T., Ashina, T., Fujiyoshi, Y., Kume, N., Yamagishi, H., Nakai, M., (1994). Projection structures of human immunodeficiency virus type 1 (HIV-1) observed with high resolution electron cryo-microscopy. *J. Electron Microsc.* 43, 16–19.
- Kewalramani, V.N., Emerman, M., (1996). Vpx association with mature core structures of HIV-2. Virology 218, 159– 168.
- Martin, J.L., Cao, S., Maldonado, J.O., Zhang, W., Mansky, L.M., (2016). Distinct particle morphologies revealed

- through comparative parallel analyses of retrovirus-like particles. *J. Virol.* **90**, 8074–8084.
- Freed, E.O., (2015). HIV-1 assembly, release and maturation. *Nature Rev. Microbiol.* 13, 484–496.
- Hanson, H.M., Willkomm, N.A., Yang, H., Mansky, L.M., (2022). Human Retrovirus Genomic RNA Packaging. Viruses 14, 1094.
- Gamble, T.R., Vajdos, F.F., Yoo, S., Worthylake, D.K., Houseweart, M., Sundquist, W.I., et al., (1996). Crystal structure of human cyclophilin A bound to the aminoterminal domain of HIV-1 capsid. *Cell* 87, 1285–1294.
- Gamble, T.R., Yoo, S., Vajdos, F.F., von Schwedler, U.K., Worthylake, D.K., Wang, H., et al., (1997). Structure of the carboxyl-terminal dimerization domain of the HIV-1 capsid protein. *Science* 278, 849–853.
- Momany, C., Kovari, L.C., Prongay, A.J., Keller, W., Gitti, R.K., Lee, B.M., et al., (1996). Crystal structure of dimeric HIV-1 capsid protein. *Nature Struct. Biol.* 3, 763–770.
- Li, Y.L., Chandrasekaran, V., Carter, S.D., Woodward, C. L., Christensen, D.E., Dryden, K.A., et al., (2016). Primate TRIM5 proteins form hexagonal nets on HIV-1 capsids. *eLife*.
- Wagner, J.M., Roganowicz, M.D., Skorupka, K., Alam, S. L., Christensen, D., Doss, G., et al., (2016). Mechanism of B-box 2 domain-mediated higher-order assembly of the retroviral restriction factor TRIM5alpha. *eLife*, 5.
- Briggs, J.A., Johnson, M.C., Simon, M.N., Fuller, S.D., Vogt, V.M., (2006). Cryo-electron microscopy reveals conserved and divergent features of gag packing in immature particles of Rous sarcoma virus and human immunodeficiency virus. *J. Mol. Biol.* 355, 157–168.
- Briggs, J.A., Riches, J.D., Glass, B., Bartonova, V., Zanetti, G., Krausslich, H.G., (2009). Structure and assembly of immature HIV. PNAS 106, 11090–11095.
- Briggs, J.A., Simon, M.N., Gross, I., Krausslich, H.G., Fuller, S.D., Vogt, V.M., et al., (2004). The stoichiometry of Gag protein in HIV-1. *Nature Struct. Mol. Biol.* 11, 672–675.
- Maldonado, J.O., Cao, S., Zhang, W., Mansky, L.M., (2016). Distinct Morphology of Human T-Cell Leukemia Virus Type 1-Like Particles. Viruses 8
- Wright, E.R., Schooler, J.B., Ding, H.J., Kieffer, C., Fillmore, C., Sundquist, W.I., et al., (2007). Electron cryotomography of immature HIV-1 virions reveals the structure of the CA and SP1 Gag shells. *EMBO J.* 26, 2218–2226.
- Yeager, M., Wilson-Kubalek, E.M., Weiner, S.G., Brown, P.

   Rein, A., (1998). Supramolecular organization of immature and mature murine leukemia virus revealed by electron cryo-microscopy: implications for retroviral assembly mechanisms. *PNAS* 95, 7299–7304.
- Saha, I., Preece, B., Peterson, A., Durden, H., MacArthur, B., Lowe, J., et al., (2021). Gag-Gag Interactions Are Insufficient to Fully Stabilize and Order the Immature HIV Gag Lattice. Viruses 13
- Schur, F.K., Obr, M., Hagen, W.J., Wan, W., Jakobi, A.J., Kirkpatrick, J.M., et al., (2016). An atomic model of HIV-1 capsid-SP1 reveals structures regulating assembly and maturation. *Science* 353, 506–508.
- Dick, R.A., Zadrozny, K.K., Xu, C., Schur, F.K.M., Lyddon, T.D., Ricana, C.L., et al., (2018). Inositol phosphates are assembly co-factors for HIV-1. *Nature* 560, 509–512.
- Adams, P.D., Afonine, P.V., Bunkoczi, G., Chen, V.B., Davis, I.W., Echols, N., et al., (2010). PHENIX: a comprehensive Python-based system for macromolecular

- structure solution. *Acta Crystallogr. D Biol. Crystallogr.* **66**, 213–221.
- Highland, C.M., Tan, A., Ricana, C.L., Briggs, J.A.G., Dick, R.A., (2023). Structural insights into HIV-1 polyaniondependent capsid lattice formation revealed by single particle cryo-EM. *Proc. Natl. Acad. Sci. USA* 120 e2220545120.
- Mattei, S., Glass, B., Hagen, W.J., Krausslich, H.G., Briggs, J.A., (2016). The structure and flexibility of conical HIV-1 capsids determined within intact virions. *Science* 354, 1434–1437.
- Ni, T., Zhu, Y., Yang, Z., Xu, C., Chaban, Y., Nesterova, T., et al., (2021). Structure of native HIV-1 cores and their interactions with IP6 and CypA. Sci. Adv. 7, eabj5715.
- Schirra, R.T., Dos Santos, N.F.B., Zadrozny, K.K., Kucharska, I., Ganser-Pornillos, B.K., Pornillos, O., (2023). A molecular switch modulates assembly and host factor binding of the HIV-1 capsid. *Nature Struct. Mol. Biol.* 30, 383–390.
- Zhao, G., Perilla, J.R., Yufenyuy, E.L., Meng, X., Chen, B., Ning, J., et al., (2013). Mature HIV-1 capsid structure by cryo-electron microscopy and all-atom molecular dynamics. *Nature* 497, 643–646.
- Ni, T., Gerard, S., Zhao, G., Dent, K., Ning, J., Zhou, J., et al., (2020). Intrinsic curvature of the HIV-1 CA hexamer underlies capsid topology and interaction with cyclophilin A. *Nature Struct. Mol. Biol.* 27, 855–862.
- Price, A.J., Marzetta, F., Lammers, M., Ylinen, L.M.J., Schaller, T., Wilson, S.J., Towers, G.J., James, L.C., (2009). Active site remodeling switches HIV specificity of antiretroviral TRIMCyp. *Nature Struct. Mol. Biol.* 16, 1036– 1042
- Rosenthal, P.B., Henderson, R., (2003). Optimal determination of particle orientation, absolute hand, and contrast loss in single-particle electron cryomicroscopy. *J. Mol. Biol.* 333, 721–745.
- Gres, A.T., Kirby, K.A., KewalRamani, V.N., Tanner, J.J., Pornillos, O., Sarafianos, S.G., (2015). STRUCTURAL VIROLOGY. X-ray crystal structures of native HIV-1 capsid protein reveal conformational variability. Science 349, 99– 103
- Pornillos, O., Ganser-Pornillos, B.K., Yeager, M., (2011).
   Atomic-level modelling of the HIV capsid. *Nature* 469, 424–427.
- Worthylake, D.K., Wang, H., Yoo, S., Sundquist, W.I., Hill, C.P., (1999). Structures of the HIV-1 capsid protein dimerization domain at 2.6 A resolution. *Acta Crystallogr.* D Biol. Crystallogr. 55, 85–92.
- 44. Mattei, S., Tan, A., Glass, B., Muller, B., Krausslich, H.G., Briggs, J.A.G., (2018). High-resolution structures of HIV-1 Gag cleavage mutants determine structural switch for virus maturation. *Proc. Natl. Acad. Sci. USA* 115, E9401–E9410.
- Scaramuzza, S., Castano-Diez, D., (2021). Step-by-step guide to efficient subtomogram averaging of virus-like particles with Dynamo. *PLoS Biol.* 19, e3001318.
- 46. Castano-Diez, D., Kudryashev, M., Stahlberg, H., (2017). Dynamo Catalogue: Geometrical tools and data management for particle picking in subtomogram averaging of cryo-electron tomograms. *J. Struct. Biol.* 197, 135–144.
- Zivanov, J., Oton, J., Ke, Z., von Kugelgen, A., Pyle, E., Qu, K., et al., (2022). A Bayesian approach to singleparticle electron cryo-tomography in RELION-4.0. *eLife*, 11.

- Louis, J.M., Ishima, R., Aniana, A., Sayer, J.M., (2009). Revealing the dimer dissociation and existence of a folded monomer of the mature HIV-2 protease. *Protein Sci.* 18, 2442–2453.
- Carlson, L.A., Briggs, J.A., Glass, B., Riches, J.D., Simon, M.N., Johnson, M.C., et al., (2008). Three-dimensional analysis of budding sites and released virus suggests a revised model for HIV-1 morphogenesis. *Cell Host Microbe* 4, 592–599.
- Pak, A.J., Grime, J.M.A., Sengupta, P., Chen, A.K., Durumeric, A.E.P., Srivastava, A., et al., (2017). Immature HIV-1 lattice assembly dynamics are regulated by scaffolding from nucleic acid and the plasma membrane. *Proc. Natl. Acad. Sci. USA* 114, E10056–E10065.
- Dick, R.A., Xu, C., Morado, D.R., Kravchuk, V., Ricana, C. L., Lyddon, T.D., et al., (2020). Structures of immature EIAV Gag lattices reveal a conserved role for IP6 in lentivirus assembly. *PLoS Pathog.* 16, e1008277.
- Qu, K., Glass, B., Dolezal, M., Schur, F.K.M., Murciano, B., Rein, A., et al., (2018). Structure and architecture of immature and mature murine leukemia virus capsids. *Proc. Natl. Acad. Sci. USA* 115, E11751–E11760.
- Obr, M., Schur, F.K.M., Dick, R.A., (2021). A Structural Perspective of the Role of IP6 in Immature and Mature Retroviral Assembly. *Viruses*, 13.
- Campbell, S., Fisher, R.J., Towler, E.M., Fox, S., Issaq, H. J., Wolfe, T., et al., (2001). Modulation of HIV-like particle assembly in vitro by inositol phosphates. *Proc. Natl. Acad. Sci. USA* 98, 10875–10879.
- Mallery, D.L., Kleinpeter, A.B., Renner, N., Faysal, K.M.R., Novikova, M., Kiss, L., et al., (2021). A stable immature lattice packages IP6 for HIV capsid maturation. Sci. Adv.,
- Yang, H., Talledge, N., Arndt, W.G., Zhang, W., Mansky, L. M., (2022). Human immunodeficiency virus type 2 capsid protein mutagenesis reveals amino acid residues important for virus particle assembly. *J. Mol. Biol.* 434, 167753.
- 57. Kleinpeter, A.B., Freed, E.O., (2020). HIV-1 Maturation: Lessons Learned from Inhibitors. *Viruses* 12, 940.
- Li, F., Goila-Gaur, R., Salzwedel, K., Kilgore, N.R., Reddick, M., Matallana, C., et al., (2003). PA-457: a potent HIV inhibitor that disrupts core condensation by targeting a late step in Gag processing. *Proc. Natl. Acad.* Sci. USA 100, 13555–13560.
- Purdy, M.D., Shi, D., Chrustowicz, J., Hattne, J., Gonen, T., Yeager, M., (2018). MicroED structures of HIV-1 Gag CTD-SP1 reveal binding interactions with the maturation inhibitor bevirimat. *Proc. Natl. Acad. Sci. USA* 115, 13258–13263.
- Sarkar, S., Zadrozny, K.K., Zadorozhnyi, R., Russell, R.W., Quinn, C.M., Kleinpeter, A., et al., (2023). Structural basis of HIV-1 maturation inhibitor binding and activity. *Nature Commun.* 14, 1237.
- Martin, J.L., Mendonca, L.M., Angert, I., Mueller, J.D., Zhang, W., Mansky, L.M., (2017). Disparate Contributions of Human Retrovirus Capsid Subdomains to Gag-Gag Oligomerization, Virus Morphology, and Particle Biogenesis. J. Virol. 91
- Emsley, P., Lohkamp, B., Scott, W.G., Cowtan, K., (2010).
   Features and development of Coot. Acta Crystallogr. D Biol. Crystallogr. 66, 486–501.
- Li, X., Mooney, P., Zheng, S., Booth, C.R., Braunfeld, M.B., Gubbens, S., et al., (2013). Electron counting and beaminduced motion correction enable near-atomic-resolution single-particle cryo-EM. *Nature Methods* 10, 584–590.

- 64. Zhang, K., (2016). Gctf: Real-time CTF determination and correction. *J. Struct. Biol.* 193, 1–12.
- Scheres, S.H., (2016). Processing of Structurally Heterogeneous Cryo-EM Data in RELION. Methods Enzymol. 579, 125–157.
- Zivanov, J., Nakane, T., Forsberg, B.O., Kimanius, D., Hagen, W.J., Lindahl, E., et al., (2018). New tools for automated high-resolution cryo-EM structure determination in RELION-3. *Elife*, 7.
- Kremer, J.R., Mastronarde, D.N., McIntosh, J.R., (1996).
   Computer visualization of three-dimensional image data using IMOD. J. Struct. Biol. 116, 71–76.
- Chen, M., Bell, J.M., Shi, X., Sun, S.Y., Wang, Z., Ludtke, S.J., (2019). A complete data processing workflow for cryo-

- ET and subtomogram averaging. *Nature Methods* **16**, 1161–1168.
- Rohou, A.G.N., (2015). CTFFIND4: Fast and accurate defocus estimation from electron micrographs. *J. Struct. Biol.* 192, 216–221.
- Castano-Diez, D., Kudryashev, M., Arheit, M., Stahlberg, H., (2012). Dynamo: a flexible, user-friendly development tool for subtomogram averaging of cryo-EM data in highperformance computing environments. *J. Struct. Biol.* 178, 139–151.
- Pettersen, E.F., Goddard, T.D., Huang, C.C., Couch, G.S., Greenblatt, D.M., Meng, E.C., et al., (2004). UCSF Chimera–a visualization system for exploratory research and analysis. *J. Comput. Chem.* 25, 1605–1612.